Pergamon

Acta mater. 49 (2001) 3029–3038

Acta MATERIALIA

www.elsevier.com/locate/actamat

APPLICATION OF THE KOCKS–MECKING MODEL TO TENSILE DEFORMATION OF AN AUSTENITIC 25Cr–19Ni STEEL

N. TSUCHIDA[1], Y. TOMOTA[2]†, H. MORIYA[3], O. UMEZAWA[4] and K. NAGAI[4]

[1]Ibaraki University, 4-12-1, Nakanarusawa, 316-8511, Hitachi, Japan, [2]Department of Materials Science, Faculty of Engineering, Ibaraki University, 4-12-1, Nakanarusawa, 316-8511, Hitachi, Japan, [3]Corporate R&D Center, Mitsui Mining & Smelting Co., Ltd, 1333-2, Haraichi, 362-0021, Ageo, Japan and [4]Materials Engineering Laboratory, National Institute for Materials Science, 1-2-1, Sengen, 305-0047, Tsukuba, Japan

(Received 7 March 2001; accepted 8 May 2001)

Abstract—Stress–strain relationships obtained by tensile test below room temperature for an austenitic 25Cr–19Ni steel were analyzed by using the Kocks–Mecking model to make clear the effects of temperature and strain rate on flow stress. A temperature range used here is between 77 and 296 K, a strain rate range between 10^{-9} and 10^{-2} s^{-1} and true strain below 0.2, where structure evolution depends on strain but scarcely on temperature and strain rate. This means that work-hardening rate is almost independent of test temperature and strain rate in the above ranges. Crosshead-arresting tests were performed to obtain flow stresses at 10^{-9} s^{-1} and the results suggested that the athermal stress could hardly be determined from the measurement of stress relaxation behavior at low temperatures. Flow curves obtained by the above deforming conditions are successfully described by using the Kocks–Mecking model with minor modifications. That is, we have claimed that the work-hardening consists of the thermal stress and the athermal stress. It should be noted that the flow curves for as hot-rolled specimens and for annealed specimens can be well simulated by changing the athermal stress.

Keywords: Steels, austenite; Kocks–Mecking model

1. INTRODUCTION

The deformation behavior of metals and alloys has been investigated experimentally and theoretically by many workers. In modeling to understand the effects of temperature and strain rate on flow stress, Kocks [1] has proposed an empirical work-hardening law from the viewpoint of work-hardening rate (Θ) versus stress (σ) relation based on thermal activation process for dislocation density evolution. This work-hardening law has been developed to describe σ-strain (ε) curves by Mecking and Kocks [2] and Follansbee and Kocks [3], i.e., the so-called Kocks–Mecking (KM) model. The KM model has been applied to several metals and alloys so far, for example, Cu [3], Al [4], Ni–C alloys [5] and Ti alloys [6–8]. The features of the KM model include (1) superposition of different thermal activation barriers for dislocation motion and (2) evaluation of work-hardening associated with dislocation accumulation and recovery principally based on the Voce law [9]. This work-hardening law corresponds to the stage III of plastic deformation in a polycrystalline material. We have examined the KM model and a single barrier activation model [10] for a Ti–Fe–O alloy and have found that the KM model is more appropriate to describe σ–ε curves at temperatures between 77 and 296 K and strain rates between 10^{-9} and 10^{-2} s^{-1} [8]. The application of the KM model to austenitic steels has not been investigated yet although Kocks studied work-hardening behaviour in an 18-8 stainless steel in his earlier paper [1]. This may be because some austenitic steels are metastable so that stress-induced martensitic transformation may intrude during deformation. In this study, tensile tests were performed for a stable austenitic stainless steel and the application of the KM model was investigated. As a result, the KM model is revealed satisfactorily to describe σ–ε relations obtained by tensile and creep deformations below room temperature when tensile strain is limited below 0.2. This paper describes the results obtained by tensile test and those by creep test will be reported in another paper [11].

† To whom all correspondence should be addressed. Tel.: +81-294-38-5055; fax: +81-294-38-5226.

E-mail address: tomota@ipc.ibaraki.ac.jp (Y. Tomota)

1359-6454/01/$20.00
PII: S1359-6454(01)00197-5

2. OUTLINE OF THE KOCKS–MECKING MODEL EMPLOYED

The KM model has been used with some modifications depending on a material examined. Here, flow stress σ is described as a function of test temperature (T), strain rate ($\dot{\varepsilon}$) and true strain (ε) as follows,

$$\frac{\sigma}{\mu} = \frac{\hat{\sigma}_a}{\mu} + s_I(\dot{\varepsilon},T)\frac{\hat{\sigma}_I}{\mu_0} + s_D(\dot{\varepsilon},T)\frac{\hat{\sigma}_D}{\mu_0} \tag{1}$$

where μ is temperature-dependent shear modulus [12] and μ_0 the shear modulus at 0 K. The first term of the right hand side, $\hat{\sigma}_a$, is athermal stress which means the yield stress at a temperature above the critical temperature, T_c. Although $\hat{\sigma}_a$, is usually regarded as a material constant, it is expressed as a function of strain for the present steel; work-hardening contains the athermal stress. The second and third terms mean two different kinds of obstacles for dislocation motion accompanying relevant thermal activation mechanisms; the second term refers to yielding, i.e., Peierls potential barrier and solid solution hardening, where the mechanical threshold stress, $\hat{\sigma}_I$, is lowered with thermal activation by factor s_I ($\dot{\varepsilon}$,T); in the third term $\hat{\sigma}_D$, is a threshold stress to overcome a barrier caused by dislocation–dislocation interactions, which is also decreased by s_D ($\dot{\varepsilon}$, T). To be noted here is that $\hat{\sigma}_D$ is increased during deformation by increasing of dislocation density that depends on temperature and strain rate because dynamic recovery takes place.

The following equations are frequently used for s_I($\dot{\varepsilon}$, T) and s_D ($\dot{\varepsilon}$, T), respectively [3],

$$s_I(\dot{\varepsilon},T) = \left[1-\left(\frac{kT}{g_{0I}\mu b^3}\ln\frac{\dot{\varepsilon}_{0I}}{\dot{\varepsilon}}\right)^{\frac{1}{q_I}}\right]^{\frac{1}{P_I}} \tag{2}$$

$$s_D(\dot{\varepsilon},T) = \left[1-\left(\frac{kT}{g_{0D}\mu b^3}\ln\frac{\dot{\varepsilon}_{0D}}{\dot{\varepsilon}}\right)^{\frac{1}{q_D}}\right]^{\frac{1}{P_D}} \tag{3}$$

where g_0, $\dot{\varepsilon}_0$, q and p are constants and their suffixes I and D refer to yielding and work-hardening, respectively. The threshold stress $\hat{\sigma}_D$ increases with strain as the dislocation substructure evolves due to dislocation accumulation and annihilation, which is connected with the work-hardening law proposed by Kocks [1],

$$\hat{\sigma}_D = \hat{\sigma}_{Ds}\left[1-\exp\left(\frac{-\Theta_0\varepsilon}{\hat{\sigma}_{Ds}}\right)\right] \tag{4}$$

Here, Θ_0 means the stage II work-hardening rate and $\hat{\sigma}_{Ds}$, the saturation stress of $\hat{\sigma}_D$ at an arbitrary temperature and strain rate. Thus, $\hat{\sigma}_{Ds}$ is associated with the saturated dislocation substructure obtained by extremely heavy plastic deformation and hence dependent on deformation condition, which cannot appear in tensile deformation because necking starts before reaching such a situation. Equation (4) is derived from the following Voce law [9],

$$\Theta = \frac{d\hat{\sigma}_D}{d\varepsilon} = \Theta_0\left[1-\frac{\hat{\sigma}_D}{\hat{\sigma}_{Ds}}\right] \tag{5}$$

where Θ means actually observed work-hardening rate at an arbitrary temperature and a strain rate, which decreases linearly with increasing of stress in the stage III deformation [1]. As was found in [1], equation (5) has frequently been examined by using the measured σ instead of $\hat{\sigma}_D$ whose ratio is given by s_D ($\dot{\varepsilon}$,T).

As mentioned above, $\hat{\sigma}_{Ds}$ is dependent on deformation temperature and strain rate because dynamic recovery is controlled by thermal activation process [3]. We should be careful about the difference between $\hat{\sigma}_{Ds}$, and actually obtained saturated stress at an arbitrary deformation condition, σ_{Ds}. That is, the saturated dislocation structure shows σ_{Ds} at a given deformation temperature and strain rate by which condition it was evolved, but would show $\hat{\sigma}_{Ds}$ if it were tested at 0 K without any help of thermal activation for dislocation motion. Influence of testing condition on $\hat{\sigma}_{Ds}$ has been investigated and given by Kocks [1] as follows:

$$\ln\frac{\hat{\sigma}_{Ds}}{\mu} = \ln\frac{\hat{\sigma}_{Ds0}}{\mu_0} - \frac{kT}{g_{0D}\mu b^3}\ln\frac{\dot{\varepsilon}_0}{\dot{\varepsilon}} \tag{6}$$

where k is Boltzmann constant, $\dot{\varepsilon}_0$ material constant and σ_{Ds0} the imaginary saturated stress if deformation were given at 0 K. The work-hardening law at arbitrary temperature and strain rate is given by combining equations (5) and (6),

$$\Theta = \Theta_0\left[1-\frac{\hat{\sigma}_{Ds}}{\hat{\sigma}_{Ds0}}\frac{\mu_0}{\mu}\left(\frac{\dot{\varepsilon}_0}{\dot{\varepsilon}}\right)^{kT/g_{0D}\mu b^3}\right] \tag{7}$$

3. EXPERIMENTAL PROCEDURES

Table 1 lists the chemical compositions of an austenitic 25Cr–19Ni steel (JIS-SUS310S) used in this study. Some of as received, i.e., commercial plates were annealed at 1373 K for 1.8 ks. Tensile test specimens with a gauge diameter of 3.5 mm and a gauge length of 25 mm were prepared from the as-received plates (material R) and the annealed plates (material A). Figure 1 shows optical and transmission electron micrographs of these two plates. As seen in (c), dislocation substructure evolved during hot-rolling remained in material R. Austenite grain size measured by the ASTM method is 64.5 μm for material R and 91.3 μm for material A. Tensile tests with strain rates

Table 1. Chemical composition of an austenitic 25Cr–19Ni steel used (mass%)

C	Si	Mn	P	S	Ni	Cr	N
0.04	0.72	1.08	0.024	0.002	19.01	24.93	0.039

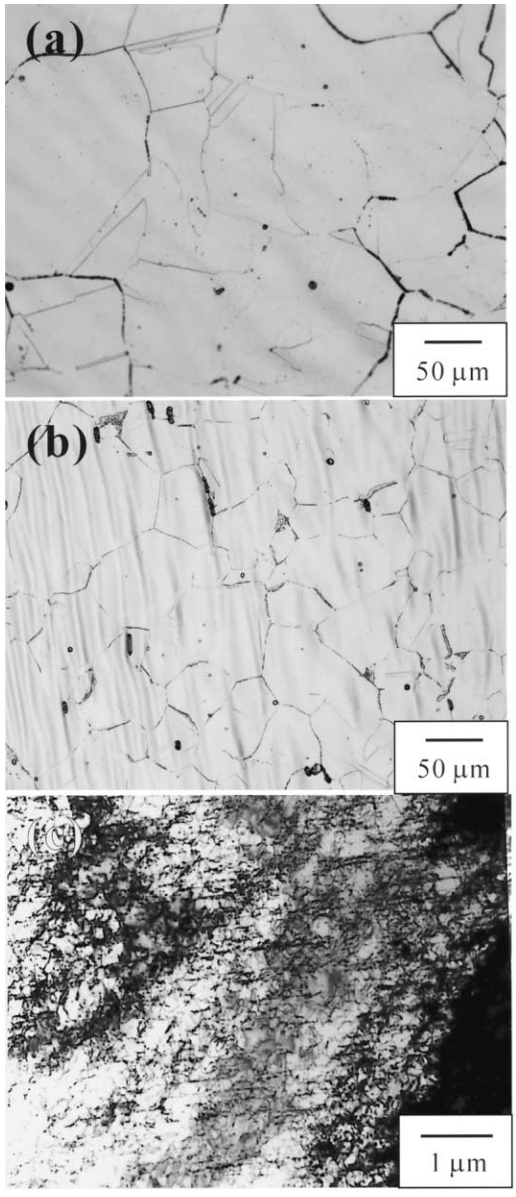

Fig. 1. Optical micrograghs (OM) and a transmission electron micrograph materials A and R: (a) A, OM, (b) R, OM and (c) R, TEM.

between 10^{-5} and 10^{-2} s^{-1} were performed at 77 K (in liquid nitrogen), 210±1 K (in methanol) and 296 K (in air) by using a gear-driven type Instron machine. An extensometer with a gauge length of 20 mm was capable of measuring displacement up to 5 mm, i.e., nominal strain of 0.25. In the crosshead-arresting test [13], changes in load and displacement were recorded while crosshead was arrested at several strains from 0.05 to 0.1 at 77, 210 and 296 K. The methods of these tests are identical with our previous study for a Ti–Fe–O alloy [13]. Discs with approximately 600 μm in thickness for transmission electron microscopy (TEM) were taken from the tensile test specimens by using a low speed saw in such a way that their flat plane was perpendicular to the tensile direction. After mechanical polishing with #1200 emery paper, TEM foils were prepared by electrical jet-polishing at 283 K in a solution of 10% acetic and 90% methanol. Microstructures were observed by using JEOL 2000FX operated at 200 kV.

4. RESULTS AND DISCUSSIONS

4.1. Flow curves obtained by the conventional tensile tests at various temperatures and strain rates

Figure 2 presents true stress (σ)–true strain (ε) curves for material A at 296, 210 and 77 K. They are dependent of test temperature and strain rate. To be noted here is that all the curves are almost parallel with respect to σ. Figure 3 shows (σ–ε) curves with an initial strain rate of 3.3×10^{-4} s^{-1} at 296 and 77 K for material R. The flow stress for material R is higher than that for material A. As seen, the flow curves are nearly parallel from each other for material R, too. These parallel shifts suggest that the influences of test temperature and strain rate on substructure evolution are negligible. That is, the influence of dynamic recovery during deformation is postulated to be almost the same within the deformation conditions employed here. If it is true, deformation substructure evolution must be similar even when either test temperature and/or strain rate are changed.

The microstructures of specimens after tensile deformation were observed by TEM. Figure 4 shows TEM microstructures for material R deformed at 296 and 77 K. When a specimen was deformed at 296 K, planar dislocations were observed as shown in (a). At 77 K, similar substructure was evolved until the tensile strain of 0.1 as is shown in (b). Figure 4(c) however reveals that deformation twinning was intruded at a higher strain at 77 K. Consequently, the substructure evolution is found to be dependent on temperature when observed in a wide strain range. But, it is almost similar when we limit our discussion within a small strain range, for instance, below 0.2. In fact, when we carefully examine the flow curves in Figs. 2 and 3, we can find the parallel shift from 296 to 77 K is lost at higher strains. This deviation must be caused by the intrusion of deformation twinning at 77 K.

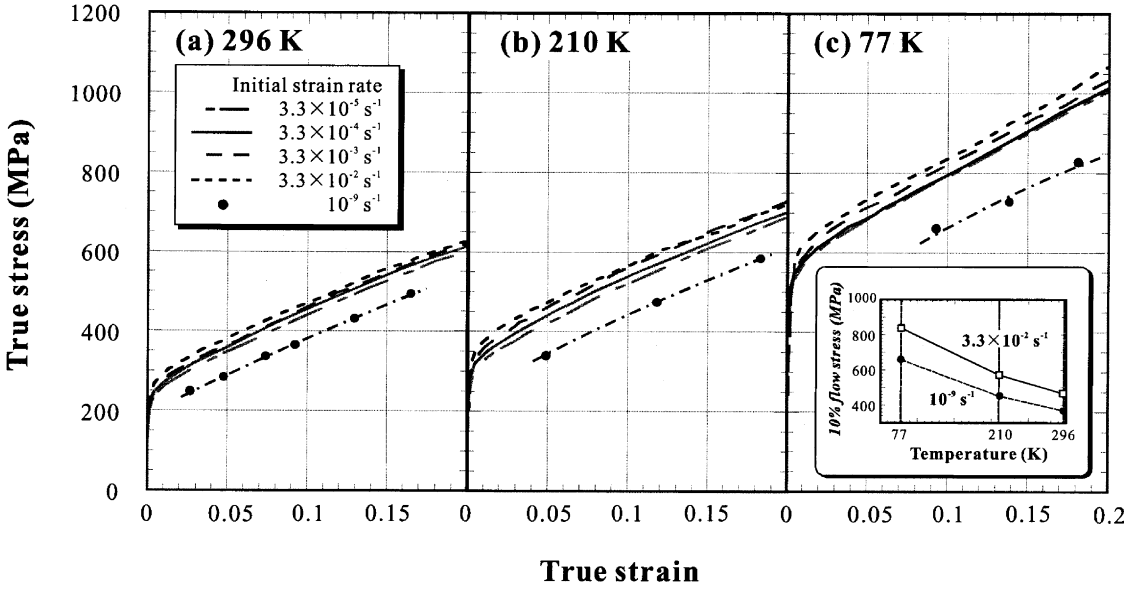

Fig. 2. True stress–true strain curves with strain rates for the material A: (a) at 296 K, (b) at 210 K, and (c) at 77 K.

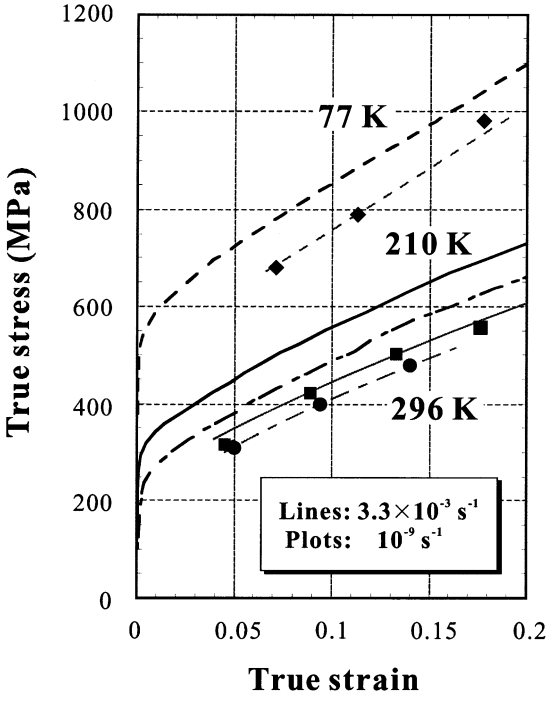

Fig. 3. True stress–true strain curves obtained with strain rate of 3.3×10^{-4} s^{-1} at 296, 210 and 77 K for the material R, in which the detectable limits of stress and strain obtained by the crosshead-arresting test were plotted.

4.2. Flow stress obtained by the crosshead-arresting test

The crosshead-arresting test [13] is a kind of stress relaxation test, by which stress at a very low strain rate can be measured. The realistic minimum strain rate was considered to be nearly 10^{-9} s^{-1} in our previous study [8]. By using a stress relaxation test, Gupta and Li [14] have determined "internal stress" which is equivalent with "athermal stress" in this paper.

Figure 5 shows stress–strain relationships obtained by the crosshead-arresting test and the conventional tensile test at 77 and 296 K. When the crosshead was temporarily stopped and kept at a fixed position, no detectable change either in load or in displacement was observed within 50 ks after holding for 360 ks as shown in Fig. 6, at which the strain rate was estimated below 10^{-9} s^{-1}. When the test was re-started after such arresting, flow stress showed a good coincidence with the flow curve obtained by the conventional continuous tensile test (see Fig. 5). This must indicate that the microstructure evolution during tensile deformation is scarcely influenced by strain rate.

If no change in stress was observed after a sufficient time for stress relaxation due to thermal activation, the applied stress should show the athermal stress which must be independent of test temperature. But as is found in Fig. 6, a large discrepancy exists between the stresses at different test temperatures after the holding of 360 ks. This result suggests strongly that the athermal stress cannot be determined from stress relaxation test for the present steel. The temperature dependence of flow stress at 10^{-9} s^{-1} was re-plotted in an inserted figure in Fig. 2. It is clear the flow stress at 10^{-9} s^{-1} depends on test temperature so that the stress–strain relationships obtained by the crosshead-arresting test are revealed to contain the thermal stress. Consequently, experimental data at higher temperatures must be needed to determine the athermal stress hence the crosshead-arresting test cannot provide the athermal stress for the present steel. Nevertheless, the stress–strain

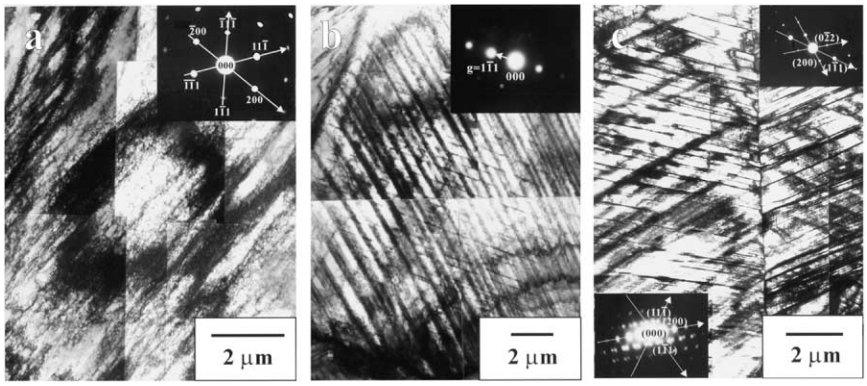

Fig. 4. TEM micrograghs for the material R after tensile deformation: (a) deformed by 20 % at 296 K, (b) deformed by 10 % at 77 K (b) and (c) deformed by 20 % at 77 K.

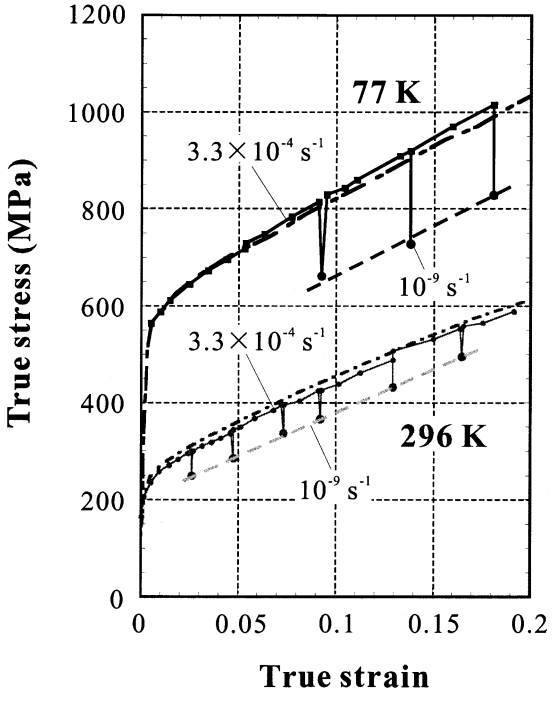

Fig. 5. True stress–true strain relationships obtained by the crosshead-arresting test and the conventional tensile test for the material A at 296 and 77 K.

relationships at the strain rate of 10^{-9} s^{-1} are of use to determine the several parameters in the KM model as will be discussed later.

4.3. Application of the KM model

By putting $T = 0$ K in equation (1), the mechanical threshold stress is given by the following three stresses:

$$\hat{\sigma} = \hat{\sigma}_a + \hat{\sigma}_I + \hat{\sigma}_D \tag{8}$$

Here, the thermal stress is separated into two components, i.e., yielding (mainly dislocation–interstitials interactions in this steel), $\hat{\sigma}_I$, and work-hardening

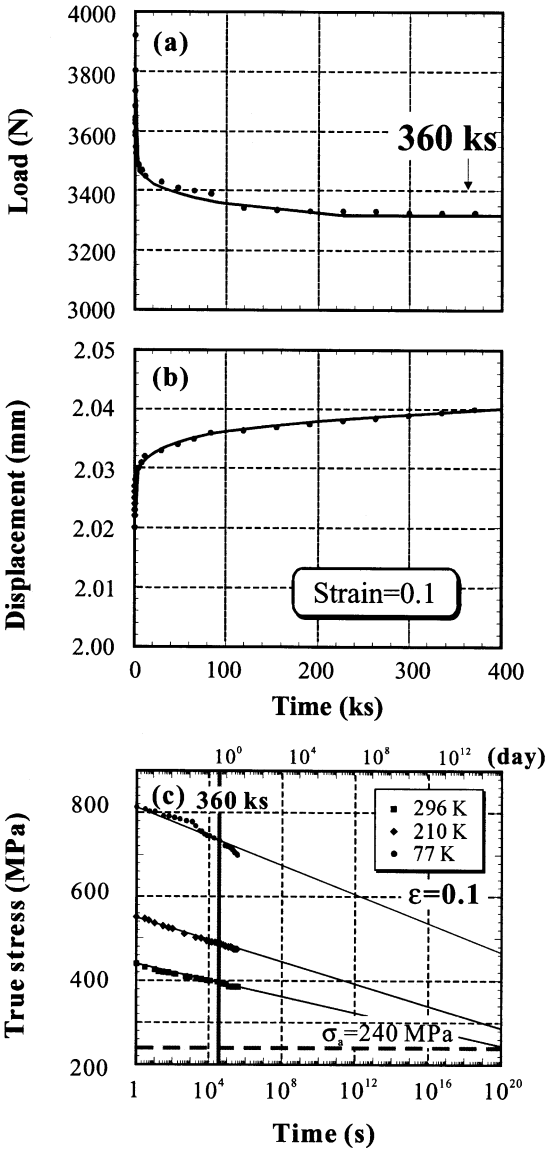

Fig. 6. Change in load (a), displacement (b) and true stress at the crosshead-arresting test for the material A at $\varepsilon \approx 0.1$ to compare with athermal stress.

(dislocation–dislocation interaction), $\hat{\sigma}_D$ that depends on strain.

The $\hat{\sigma}_I$ and $\hat{\sigma}_D$ are influenced by the values of p and q as discussed by Follansbee and Kocks [3]. Ono [15] has examined eight potentials associated with various theoretical models which give different p and q. As a result, he concluded that a pair of $p = 0.5$ and $q = 1.5$ is the most appropriate to figure the observed σ–T relationship and that it is difficult to clarify which hardening theory is correct from comparison with measured results. The pair of $p = 0.5$ and $q = 1.5$ was thereby chosen in the present analysis commonly for $\hat{\sigma}_I$ and $\hat{\sigma}_D$.

As mentioned above, the stress–relaxation tests below room temperature are considered of no use to determine $\hat{\sigma}_a$, in the present steel. Ogawa *et al.* [10] have utilized the following Larson–Miller parameter (ξ) [16] to determine $\hat{\sigma}_a$ for various Ti alloys.

$$\xi = T(\ln\dot{\varepsilon}_0 - \ln\dot{\varepsilon}) \tag{9}$$

where $\ln(\dot{\varepsilon}_0)$ was assumed to be 20 as will be explained later. Although Ogawa *et al.* had estimated $\hat{\sigma}_a$ from a L-M parameter at 15,000, we used 20,000 taking several experimental results into consideration [8]. Figure 7 shows flow stresses at several strains as a function of ξ for material A. As is apparently seen, the extrapolations of these flow stresses toward high temperature do not coincide even at $\xi = 20{,}000$, being different from the case of the Ti alloy [8]. This means that $\hat{\sigma}_a$ increases with strain although it was given as a material constant for several alloys, for instance, in Cu [3] and Ti–Fe–O alloy [8]. In the present analysis, $\hat{\sigma}_a$ was expressed by

$$\hat{\sigma}_a = 110 + 1300\varepsilon \ \text{MPa} \tag{10}$$

for material A, while

$$\hat{\sigma}_a = 150 + 1300\varepsilon \ \text{MPa} \tag{11}$$

for material R from fitting of extrapolated experimental data. It should be noted that the difference in $\hat{\sigma}_a$ for these two materials is 40 MPa being independent of strain. As usual, the work-hardening contributes to increasing the thermal stress in the KM model [3, 6, 8], but the work-hardening in the present steel is believed to consist of the thermal stress and the athermal stress. Such a difference may stem from the planar dislocation substructure due to low stacking fault energy in the present steel (see Fig. 4).

The values of $\dot{\varepsilon}_{0I}$ and $\dot{\varepsilon}_{0D}$ are associated with the maximum dislocation velocity. Here, according to Sleeswyk's analysis [17], we put $\dot{\varepsilon}_{0I} = \dot{\varepsilon}_{0D} = 10^8\ \text{s}^{-1}$, thereby $\ln(\dot{\varepsilon}_0) = 18.4$ (approximately 20).

In order to evaluate the $\hat{\sigma}_I$, plots of $(\sigma - \hat{\sigma}_a)$ as a function of temperature and strain rate like Fig. 8 are utilized. The $\hat{\sigma}_I$ was determined from the intersection of the fitting line for experimental data with the vertical axis ($T = 0$ K), while the value of g_{0I} was obtained from the slope of the fitting line. The obtained values

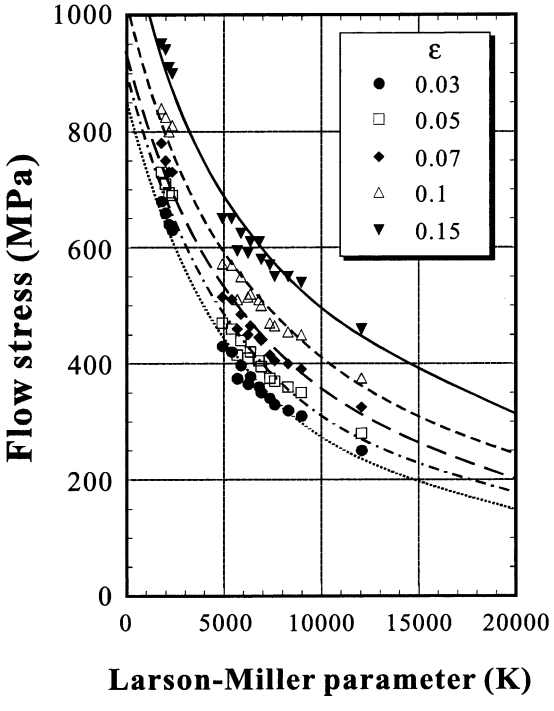

Fig. 7. Flow stress at several strains as a function of the Larson–Miller parameter (ξ) for the material A.

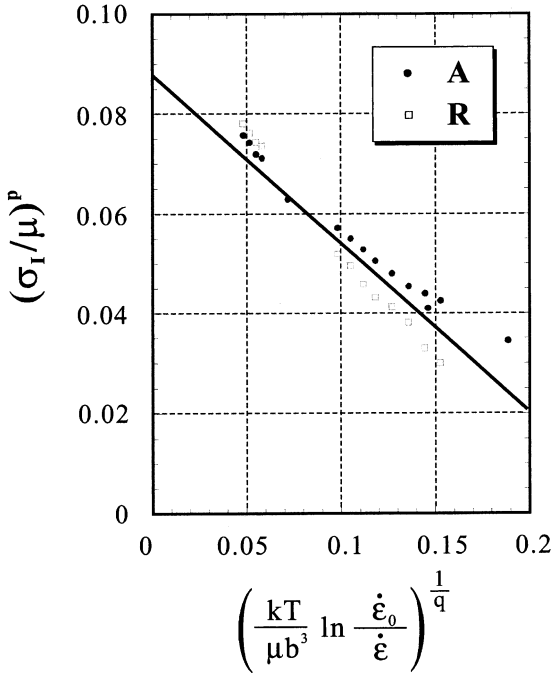

Fig. 8. Variation of the yield stress with test temperature and strain rate for the material A. The results are plotted by using equations (1) and (2).

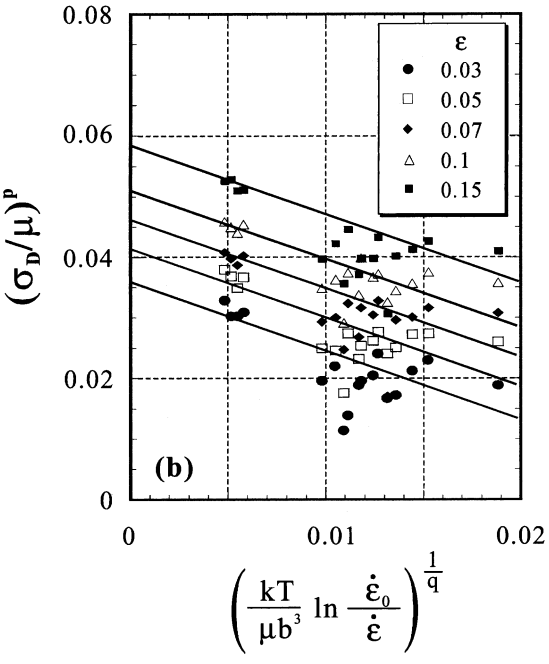

Fig. 9. Variation of the flow stress at several strains with test temperature and strain rate for the material A. The results are plotted by using equations (1) and (3).

Table 2. Shear modulus used for the calculations [12]

Temperature (K)	μ (GPa)
0	93.2
77	90.8
210	84.7
243	83.3
296	81.2

for material A are, $\hat{\sigma}_I = 680$ MPa and $g_{0I} = 0.17$. When we made similar plots for material R, we obtained almost the same results so that these values were commonly used in materials A and R.

The parameters which appear in equations (3) and (4) can be determined by using equations (5)–(7). Figure 9 shows $\sigma_D(= \sigma - \hat{\sigma}_a - s(T,\dot{\varepsilon})\hat{\sigma}_I)$ at several strains as a function of temperature and strain rate. The slope of the plots provides the value of g_{0D} and then we obtained $g_{0D} = 0.26$.

Figure 10(a) shows $(d\sigma_D/d\varepsilon)$ versus σ_D relationships at 77, 210 and 296 K. In this case, the athermal stress contributed the work-hardening as seen in equations (10) and (11) so that the work-hardening rate minus $(d\sigma_a/d\varepsilon)$ must be used to analyze the work-hardening for σ_D. At the beginning of deformation, $(d\sigma_D/d\varepsilon)$ shows an extremely high value associated with grain to grain yielding (the stage I and II). After that, a linear relation is observed for each deformation condition indicating that equation (5) holds. The $(d\sigma_D/d\varepsilon)$ at $\sigma_D = 0$ of the relevant linear fitting has been considered to show the so-called stage II hardening rate Θ_0 [1]. Thus, we obtained $\Theta_0 = 1600$ MPa. The saturation stress at 0 K, σ_{Ds0}, is found from the plotting based on equation (6) as shown in Fig. 10(b). As a result, we obtained $\sigma_{Ds} = 840$ MPa.

All the parameters of the KM model obtained for materials A and R are tabulated in Tables 2 and 3. Using these parameters, we computed flow curves at various test temperatures and strain rates. Some

Table 3. The parameters in the Kocks-Mecking model for the austenitic 25Cr–19Ni steel

Parameter	Value	
σ_a	A (as-annealed) 110+1300ε (MPa)	R (as-rolled) 150+1300ε (MPa)
g_{0I}	0.17	
p_I	0.5	
q_I	1.5	
$\hat{\sigma}_I$	680 (MPa)	
g_{0D}	0.26	
p_D	0.5	
q_D	1.5	
$\hat{\sigma}_{Ds}$	840 (MPa)	
Θ_0	1600 (MPa)	
$\dot{\varepsilon}_{0I}$	10^8	
$\dot{\varepsilon}_{0D}$	10^8	

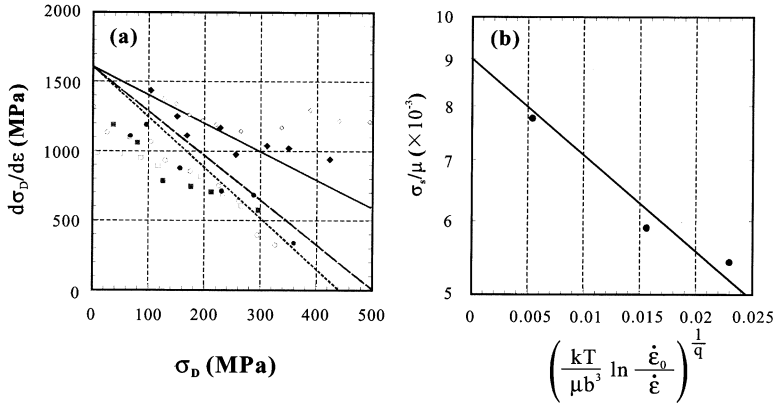

Fig. 10. (a) Work-hardening rate for the dislocation–dislocation indication $(d\sigma_D/d\varepsilon = \Theta)$ as a function of on for the materials A and R at 296, 210 and 77 K. (b) Variation of measured saturation stress as a function of temperature and strain rate.

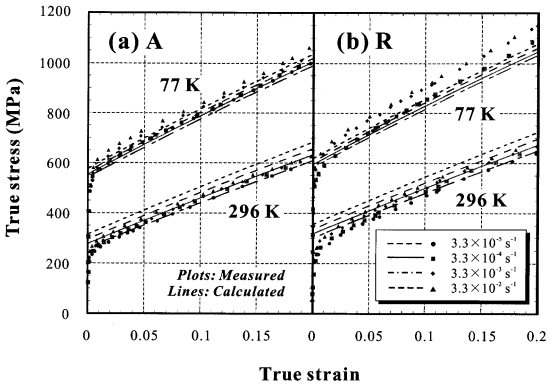

Fig. 11. Comparisons between the calculated stress–strain curves by the KM model and the measured ones at 77 and 296 K for the materials A (a) and R (b).

examples at 77 and 296 K are shown in Fig. 11. As seen σ–ε curves calculated by the KM model show good agreements with the measured ones for materials A and R. In consequence, the KM model was found satisfactorily to describe the measured σ–ε curves in the present steel. The flow curves for materials A and R can be simulated only by changing the athermal stress [equations (10) and (11)]. When we have computed a flow curve at the strain rate of 10^3 s^{-1}, the prediction showed reasonably good agreement with a curve measured by means of the Hopkinson bar method [18].

4.4. Discussions on related deformation behavior

4.4.1. Change of strain rate during tensile deformation. Flow curves at low strain rates were calculated by using the KM model so as to compare them with the measured curves obtained by the crosshead-arresting test. Figure 12 shows the results at 77 and 296 K for materials A and R where the athermal stresses were also drawn. As seen, the measured curves are consistent with the calculated curves at the strain rate of approximately 10^{-9} s^{-1}. Moreover, the measured curves are found much higher than the athermal stress.

As described above, the flow curves obtained at various conditions of test temperature and strain rate were nearly parallel below $\varepsilon = 0.2$, including the curves at 10^{-9} s^{-1}. When strain rate was changed during deformation like the crosshead-arresting test, the flow stresses before and after the strain rate change coincides with the flow curves obtained by the relevant constant strain rate tests. This means the evolution of dislocations structure is not influenced by strain rate within the examined strain rate range. In some fcc metals like Al and Cu, flow stresses with different strain rates have been reported to show the Cottrell-Stokes law in which a ratio of $(\sigma_1(\varepsilon)/\sigma_2(\varepsilon))$ is constant being independent of ε [19]. However, the flow curves with different strain rates are nearly parallel in the present steel. This is a big difference between this steel and previously reported Cu and Al. Then, a question may arise what will happen if test temperature is changed during deformation. This point is discussed in the next section.

4.4.2. Change of test temperature during tensile deformation. Concerning test temperature change during tensile deformation, two kinds of tests, T1 and T2, were carried out. In test T1, tensile deformation was stopped at $\varepsilon \approx 0.1$. Temperature was then changed from 77 to 296 K or vice versa after unloading and finally reloaded to continue tensile test at the second temperature. In test T2, the crosshead was arrested for 360 ks at $\varepsilon \approx 0.1$ at the first temperature and the following procedure was the same with test T1. The results were summarized in Fig. 13. In all cases, the flow stress at the second straining shows a good agreement with the stress obtained by the constant temperature tensile test at 77 or 296 K. The flow stress is therefore independent of deformation history so that the effect of temperature on the structure evolution is found to be of negligible order below

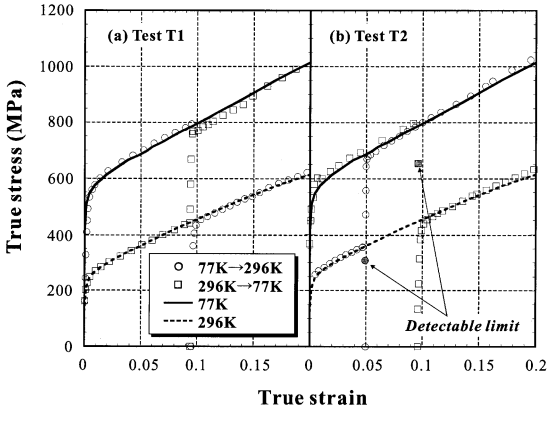

Fig. 12. Comparison between true stress–true strain relationships obtained by the conventional tensile test at 77 and 296 K and the test temperature change test for the material A: (a) test T1 and (b) test T2.

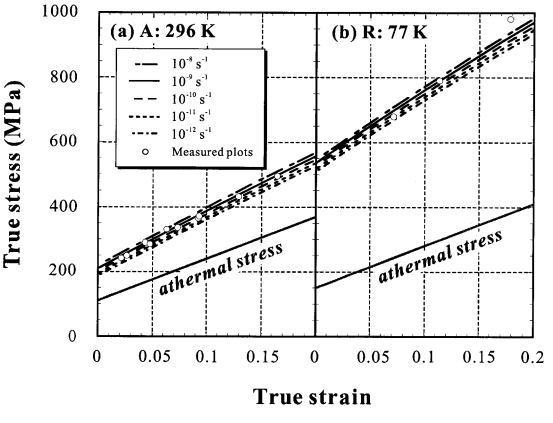

Fig. 13. Comparisons between the calculated stress–strain curves by the KM model at 77 and 296 K and the measured detectable limits obtained by the crosshead-arresting test for the materials A (a) and R (b). The athermal stress is described to compare with the detectable limits in each figure.

$\varepsilon \approx 0.2$. These results could be simulated well by the KM model. In most fcc alloys, the structure evolution is dependent on test temperature (better to say, "deformation history") even at small strains [20–22] so that such an agreement has not been observed. In the case of Al, for example, the flow stress at a lower testing temperature (the second temperature) after the first straining at a higher temperature becomes smaller than that obtained by the constant lower temperature test. In order to consider such cases in the modeling, a more detail investigation by Follansbee and Kocks [3] must be applied.

4.4.3. Features of work-hardening of the present steel. From the discussions in sections 4.4.1 and 4.4.2, the present steel seems to exhibit characteristic work-hardening behavior. To obtain more insights on this point, $(d\sigma/d\varepsilon)$ versus ε plotting was made and the result was shown in Fig. 14. It is interesting that all points gather along one curve indicating that the influences of temperature, strain rate and material condition (materials A and R) were of negligible order. The TEM observations for the deformed specimens showed that the planar dislocations structure was evolved (see Fig. 4). This result suggests that the stacking fault energy of the present steel must be relatively low and hence the cross-slip is not easy to occur resulting in little influence of testing condition on work-hardening rate below approximately $\varepsilon \approx 0.2$. If we enlarge the discussion to higher strains and/or higher temperatures, this conclusion must no longer hold. Such a deviation is found at higher strains at 77 K where the intrusion of twining increases work-hardening (see Figs 1 and 2).

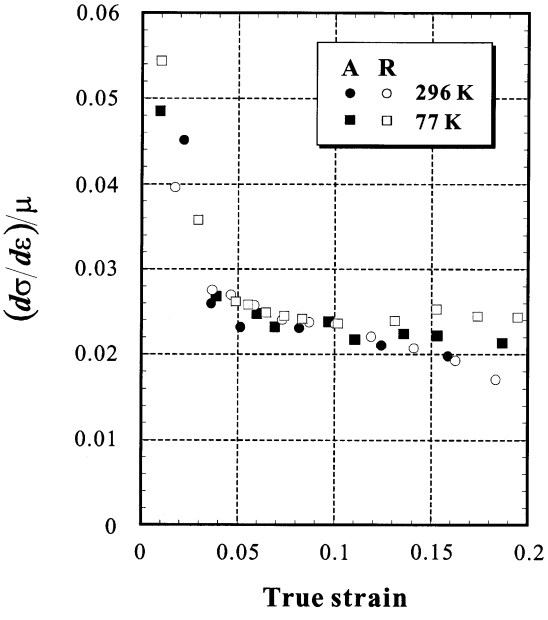

Fig. 14. Work-hardening rate $(d\sigma/d\varepsilon)$ as a function of true strain (ε) for the materials A and R at 77 and 296 K.

5. CONCLUSIONS

The effects of temperature and strain rate on the true stress (σ)-true strain (ε) relationship for hot-rolled (R) and annealed (A) conditions of an austehitic 25Cr–19Ni steel were studied by experiments and theoretical calculations. The main results obtained are the following.

1. The σ–ε curves measured at 77, 210 and 296 K with strain rates between 10^{-9} and 10^{-2} s^{-1} were almost parallel with respect to σ approximately below $\varepsilon = 0.2$.
2. According to TEM observations, microstructure evolution with tensile deformation below $\varepsilon = 0.2$ was hardly influenced by test temperature and strain rate. In the present deformation conditions, planar dislocations structure was evolved and deformation twining was intruded at 77 K at higher strains where the flow curve deviated from the parallel shift.
3. The crosshead-arresting test was found to provide the flow curve at the strain rate of 10^{-9} s^{-1} that was apparently dependent on test temperature. The athermal stress is much lower than the flow curve at 10^{-9} s^{-1} and is difficult to estimate from the stress relaxation behavior below room temperature.
4. To apply the Kocks–Mecking (KM) model to material A, the athermal stress was expressed as a function of strain, i.e., work-hardening contained athermal stress. The KM model is successfully applied to the flow curves at various test temperatures and strain rates examined below $\varepsilon \approx 0.2$, in which the flow stress at 10^{-9} s^{-1} was reasonably explained. The model was applicable to materials A and R only by changing the athermal stress.
5. Being different from the previous reports on fcc metals, the work-hardening of the present steel below $\varepsilon = 0.2$ for the present testing conditions was hardly influenced by temperature and strain rate. This must be attributed to the planar configuration of dislocations due to low stacking fault energy.

REFERENCES

1. Kocks, U. F., *J. Eng. Mater. Tech.*, 1976, **98**, 76.
2. Mecking, H. and Kocks, U. F., *Acta metall.*, 1981, **29**, 1865.
3. Follansbee, P. S. and Kocks, U. F., *Acta metall.*, 1988, **36**, 81.
4. Chu, D. and Morris, J. W. Jr., *Metall. Trans.*, 1991, **22A**, 1789.
5. Follansbee, P. S., Huang, J. C. and Gray, G. T., *Acta metall.*, 1990, **38**, 1241.
6. Chichili, D. R., Ramesh, K. T. and Hemker, K. J., *Acta mater.*, 1998, **46**, 1025.
7. Follansbee, P. S. and Gray, G. T., *Metall. Trans. A*, 1989, **2OA**, 863.
8. Tsuchida, N., Moriya, H., Tomota, Y., Umezawa, O. and Nagai, K., *ISIJ Int.*, 2000, **40**, 84.
9. Vote, E., *J. Inst. Met.*, 1948, **74**, 537.

10. Ogawa, K., *J. Soc. Mat. Sci., Japan*, 1995, **44**(501), 739.
11. Tsuchida, N., Tomota, Y., Umezawa, O., Nagai, K. and Baba, E., unpublished work.
12. Frost, H. J. and Ashby, M. F., in *Deformation Mechanism*. Pergamon Press, Oxford, 1982, p. 20.
13. Moriya, H., Nagai, K., Kawabe, Y. and Okada, A., *ISIJ Int.*, 1997, **37**, 1016.
14. Gupta, I. and Li, J. C. M., *Metall. Trans.*, 1970, **1**, 2323.
15. Ono, K., *J. Appl. Phys.*, 1968, **39**, 1803.
16. Larson, F. R. and Miller, J., *Trans. ASME*, 1952, **74**, 765.
17. Sleeswyk, A. W., *Scripta. metall.*, 1970, **4**, 355.
18. Shimizu, T. and Sakata, K., Unpublished work (ISIJ research on high speed deformation of steels for automobile use, 2000).
19. Hirsch, P. B. and Warrington, D. H., *Phil. Mag.*, 1961, **6**, 735.
20. Bullen, F. P. and Hutchison, M. M., *Phil. Mag.*, 1962, **7**, 557.
21. Adams, M. A. and Cottrell, A. H., *Phil. Mag.*, 1957, **46**, 1187.
22. Reed-Hill, R. E., Cribb, W. R. and Monteiro, S. N., *Metall. Trans.*, 1973, **4**, 2665.